ACS OMEGA

http://pubs.acs.org/journal/acsodf

Article

# Development of Mo-Modified Pseudoboehmite Supported Ni Catalysts for Efficient Hydrogen Production from Formic Acid

Liang Zheng, Zhiyu Li,* Peng Fu,* Fazhe Sun, Mingyang Liu, Tianyang Guo, and Qingwen Fan

Cite This: *ACS Omega* 2022, 7, 27172−27184

Read Online

ACCESS | Metrics & More | Article Recommendations

**ABSTRACT:** Formic acid (FA), as a safe and renewable liquid hydrogen storage material, has attracted extensive attention. In this paper, a series of Mo-modified pseudoboehmite supported Ni catalysts were developed and evaluated for efficient hydrogen production from formic acid. Pseudoboehmite (PB) as a catalyst carrier was used for the first time. Ni/PB and NiMo/PB possessed a mesostructure, and the pore size distribution was mainly concentrated between 2 and 20 nm. The oxygen vacancies caused by Mo enhanced Ni anchoring, thus inhibiting Ni sintering. Compared with Ni10/PB (7.62 nm), Ni10Mo1/PB had smaller Ni particles (5.08 nm). The Ni−O−Al solid solutions formed through the interaction of Ni with the PB improved the catalytic performance. Ni10Mo1/PB gave the highest conversion of 92.8% with a $H_2$ selectivity of 98% at 300 °C, and the catalyst activity hardly decreased during the 50 h stability test. In short, Ni10Mo1/PB was a promising catalyst for hydrogen production from formic acid because of the oxygen vacancy anchoring effect as well as the formation of Ni−O−Al solid solutions which could effectively suppress the Ni sintering.

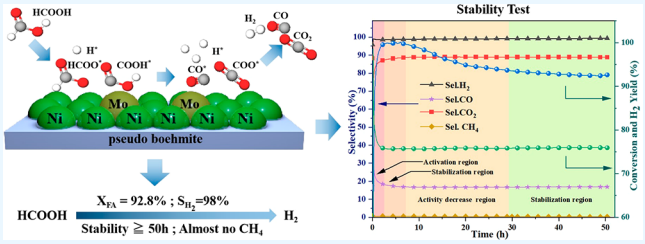


## 1. INTRODUCTION

To achieve the aim of carbon neutrality, using hydrogen energy to replace fossil fuels is an available method. At present, hydrogen energy is difficult to popularize due to the security risks in hydrogen storage and transportation. The key to solving this problem is the "hydrogen carrier", which can store and transport hydrogen efficiently.[1]

Formic acid (FA, HCOOH), a biorefinery major subproduct, is a nontoxic and cheap hydrogen carrier.[2−4] Its weight and volume $H_2$ capacity are 4.4 wt % and 53.4 g/L, respectively.[5] The ideal circulation path of formic acid as a hydrogen carrier is shown in Figure 1. The reaction of $H_2$ and $CO_2$ can produce formic acid, which is transported to a hydrogenation station to extract hydrogen and can be used for fuel cells. The $CO_2$ produced during the reaction can also be separated and recycled.[6] FA can be decomposed into $H_2$ and $CO_2$ or CO and $H_2O$ by dehydrogenation (eq 1) or dehydration (eq 2). However, the dehydration should be avoided for the purpose of hydrogen production.[7] This is because the dehydration reaction produces CO, which will reduce the activity of the catalyst.[8] It is well-known that catalysts have an important influence on the decomposition of formic acid.

$$HCOOH(l) \rightarrow H_2(g) + CO_2(g) \quad (1)$$

$$HCOOH(l) \rightarrow H_2O(l) + CO(g) \quad (2)$$

FA catalysts for hydrogen production can be divided into homogeneous and heterogeneous catalysts. Homogeneous catalysts based on organometallic complexes such as Ru,[9] Ir,[8] and Rh[10] usually have high selectivity and catalytic activity. However, the recovery of homogeneous catalysts requires special additives and organic solvents, which limits their practical application. It is easy to recover heterogeneous catalysts based on Pt,[11] Au,[12,13] and Pd,[10,14−16] but the noble metals are expensive.[17] Heterogeneous catalysts based on non-noble metals such as Ni,[18,19] Cu,[20] and Co[21] have received much attention. In addition, hydrogen production from formic acid catalyzed by non-noble metal catalysts is usually carried out in the gas phase, but the low concentration of FA has led to a low hydrogen production rate in most of the literature.[22] Therefore, it is urgent to develop a non-noble metal catalyst with high activity and strong stability for hydrogen production from high-concentration FA. Nickel-based catalysts are widely used because of their low cost and high ability to promote the formation of $H_2$ molecules.[23] The activity and stability of the catalyst can be effectively improved by selecting a suitable carrier and promoter. The catalyst carrier can interact with the active metal to change the properties of the active metal.[24] Pseudoboehmite (PB) is a layered material with high specific surface area that can interact with active metals to improve the

**Received:** March 22, 2022
**Accepted:** July 7, 2022
**Published:** July 28, 2022

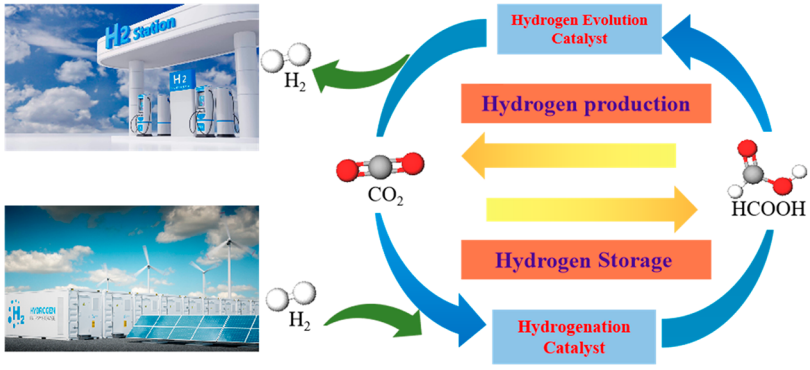


**Figure 1.** Schematic diagram of ideal hydrogen storage and the hydrogen production cycle of formic acid.

dispersion and catalytic performance of active metals. However, up to now, there have been few reports about PB as a catalyst carrier for hydrogen production from formic acid. As an excellent promoter, Mo can strengthen the interaction between the active metal and the catalyst carrier and improve the dispersibility of the active metal.[25]

In this paper, new NiMo/PB catalysts were developed for hydrogen production from formic acid, in which Ni, Mo, and PB were an active metal, promoter, and carrier, respectively. The catalysts were characterized by XRF, XRD, BET, SEM/EDX-mapping, TEM, FTIR, $H_2$-TPR, $NH_3$-TPD, and XPS to measure their physicochemical properties. The catalysts were applied to hydrogen production from formic acid in a fixed bed reactor at 300 °C to evaluate the catalytic performance. The relationship between Ni content, Ni/Mo ratio, and catalytic performance was studied, and the mechanism of formic acid decomposition was revealed.

## 2. RESULTS AND DISCUSSION

**2.1. Catalyst Characterization.** The X-ray diffraction (XRD) spectra of Ni/PB and NiMo/PB are shown in Figure 2. The peaks at 14.5°, 28.2°, 38.3°, 49.3°, 67.6°, and 72.3°

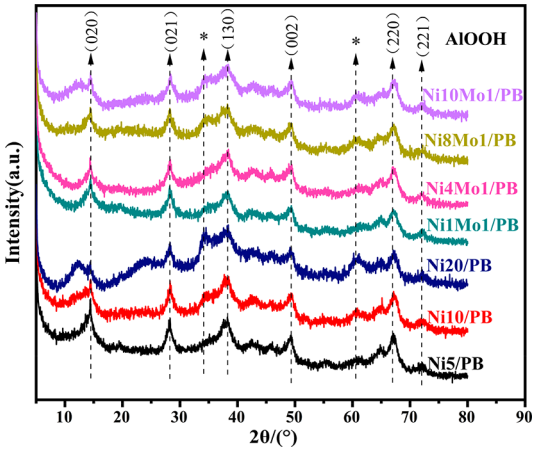


**Figure 2.** XRD patterns of Ni/PB and NiMo/PB.

belong to (020), (021), (130), (002), (220), and (221) planes of pseudoboehmite.[26] The catalysts have two special peak positions of 34.1° and 60.5°, respectively. For Ni/PB series catalysts, the peak intensity at 34.1° increases with the increase in Ni content from 5% to 20%. For NiMo/PB series catalysts, the peak at 34.1° intensity increases with the increase in NiMo ratio from 1:1 to 10:1. The peak at 60.5° shows the same phenomenon. These peaks are nickel species interacting with PB to form the Ni−O−Al solid solutions in the matrices.[27−29]

The diffraction peaks of NiO (JCPDS PDF 44-1159) with 2$\theta$ values of 37.2° (110), 43.3° (200), and 62.9° (220) were not detected. Diffraction peaks belonging to $Ni^0$ (JCPDS PDF 04-0850) with 2$\theta$ values of 44.3° (111) and 51.8° (200) were also not detected. The diffraction peaks associated with Ni and Mo species were not found in the spectra, and the same phenomenon was reported by Qian et al.[30] This can be attributed to two reasons. One is that the crystal structure of NiO and $Ni^0$ is highly amorphous, or the degree of crystallization is poor and cannot be detected by XRD. The other reason is that pseudoboehmite with a high specific surface area can promote a high dispersibility of Ni and Mo, which is beyond the detection range of XRD, indicating that Ni and Mo species with large particle sizes are not formed on pseudoboehmite.[31−33]

The $N_2$ adsorption−desorption isotherms and associated pore size distributions are shown in Figure 3. According to the classification of IUPAC, the isotherm is determined as type IV, which indicates that Ni/PB and NiMo/PB belong to a typical mesoporous material.[34,35] In addition, adsorption−desorption curves show the characteristics of an H3 type hysteresis loop. The specific surface area ($S_{BET}$) and volume ($V_p$) of Ni/PB and NiMo/PB are shown in Table 1. With an increase in the Ni/Mo ratio, $S_{BET}$ first increases and then decreases for NiMo/PB catalysts, and the Ni8Mo1/PB has the highest $S_{BET}$ (282.8 $m^2$/g). It is worth noting that the changes of $S_{BET}$ in the catalysts are accompanied by the change of the interaction between the metal and support,[36−38] which can suppress the agglomeration and sintering of active metal.[39] Therefore, the Ni/Mo ratio can change the interaction between Ni and PB, resulting in an increase in $S_{BET}$ from 273.8 $m^2$/g for Ni10Mo1-PB to 282.8 $m^2$/g for Ni8Mo1/PB and then a decrease to 199.4 $m^2$/g for Ni1Mo1/PB. Furthermore, the pore size distribution was mainly concentrated between 2 and 20 nm, and the average pore size is 5−6 nm. These results demonstrated that Ni/PB and NiMo/PB have a mesoporous structure with uniform pore size distributions.

The contents of Ni and Mo introduced into the as-prepared catalysts were determined by X-ray fluorescence (XRF) and are presented Table 1, which confirmed that the Ni and Mo were successfully loaded on PB and that the Ni and Mo contents of catalysts were almost similar to the given metal contents during catalyst preparation. Figure 4 shows the energy-dispersive X-ray spectroscopy (EDX) mapping images of Ni and Mo for Ni/PB and Ni10Mo1/PB. Ni and Mo are uniformly loaded on PB. Transmission electron microscopy (TEM) images are shown in Figure 5. For Ni10/PB, Ni agglomeration occurs, resulting in


https://doi.org/10.1021/acsomega.2c01742
ACS Omega 2022, 7, 27172−27184

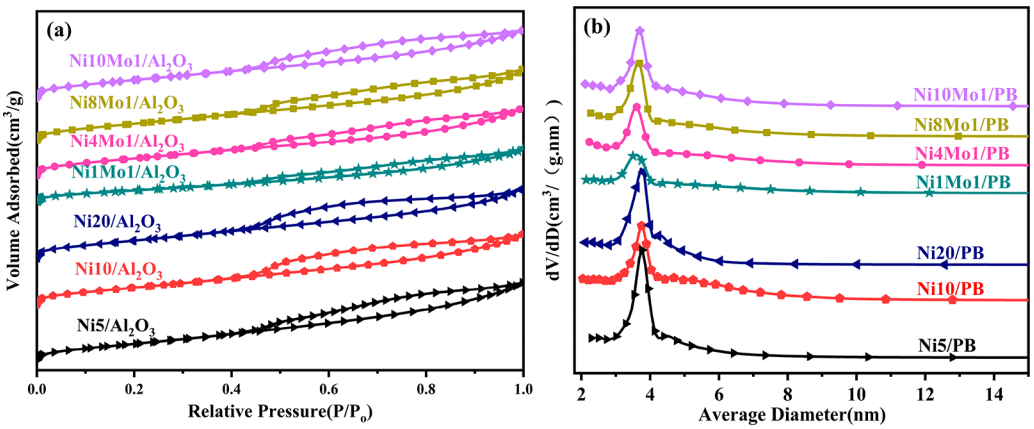


**Figure 3.** (a) $N_2$ adsorption−desorption isotherms and (b) pore distribution of Ni/PB and NiMo/PB.

**Table 1. Textural Properties of Ni/PB and NiMo/PB**

| samples | Ni content[a] (wt %) | Mo content[a] (wt %) | $S_{BET}$[b] ($m^2$/g) | $V_B$[b] ($cm^3$/g) | $D_p$[b] (nm) |
|---|---|---|---|---|---|
| Ni5/PB | 5.7 | | 283.2 | 0.48 | 6.0 |
| Ni10/PB | 10.7 | | 274.9 | 0.41 | 5.9 |
| Ni20/PB | 20.8 | | 280.8 | 0.41 | 5.7 |
| Ni1Mo1/PB | 5.3 | 4.7 | 199.4 | 0.30 | 5.9 |
| Ni4Mo1/PB | 8.8 | 1.9 | 277.3 | 0.37 | 5.6 |
| Ni8Mo1/PB | 9.5 | 1.2 | 282.8 | 0.41 | 5.7 |
| Ni10Mo1/PB | 9.7 | 0.9 | 273.8 | 0.39 | 5.3 |

[a]Obtained by XRF for catalysts. [b]Obtained by BET for catalysts.

serious sintering. Compared with Ni10/PB, the addition of Mo inhibits the occurrence of Ni agglomeration in Ni10Mo1/PB, which helps to improve the catalyst stability. From the particle size distribution histogram of Ni, Ni particles in Ni10Mo1/PB have a higher dispersibility and smaller particle size (the average Ni particle sizes in Ni10/PB and Ni10Mo1/PB are 7.62 and 5.08 nm, respectively). The addition of Mo leads to the generation of oxygen vacancies,[40] promotes the anchoring of Ni, and then inhibits the Ni sintering.

The Fourier transform infrared spectroscopy (FTIR) spectra of Ni/PB and NiMo/PB are shown in Figure 6. The peak at 1637 $cm^{-1}$ is related to the bending vibration modes of adsorbed water.[41,42] The peak at 1072 $cm^{-1}$ is attributed to the stretching vibration modes of the C−O bond. The peak at 3455 $cm^{-1}$ is related to interacting OH or to bridging OH groups.[43−45] The peak at 1395 $cm^{-1}$ is assigned to the −OH stretching vibration modes in (Al, Mg)−OH and (Fe, Mg)−OH units,[28,35] and this peak position moves to the left with an increase in Ni content, which may be attributed to the reaction of PB and Ni species to form a new species.[46] OH species can remove carbon on the catalyst surface, which can enhance the coking resistance of the catalysts and subsequently improve catalytic performance.[47] The peaks below 1000 $cm^{-1}$ are attributed to the interatomic vibrations of Ni−O.[48]

A $H_2$-temperature-programmed reduction ($H_2$-TPR) analysis was used to study the Ni/Mo reducibility and the interaction between Ni/Mo and PB. As shown in Figure 7, the inverted peak at 280 °C is attributed to the desorption of bound water. The peak at 350 °C for Ni5/PB belongs to an $\alpha$ reduction peak,[29] which is attributed to the insignificant or little interaction of NiO on PB. For Ni/PB, the peak gradually shifts to the right as the Ni

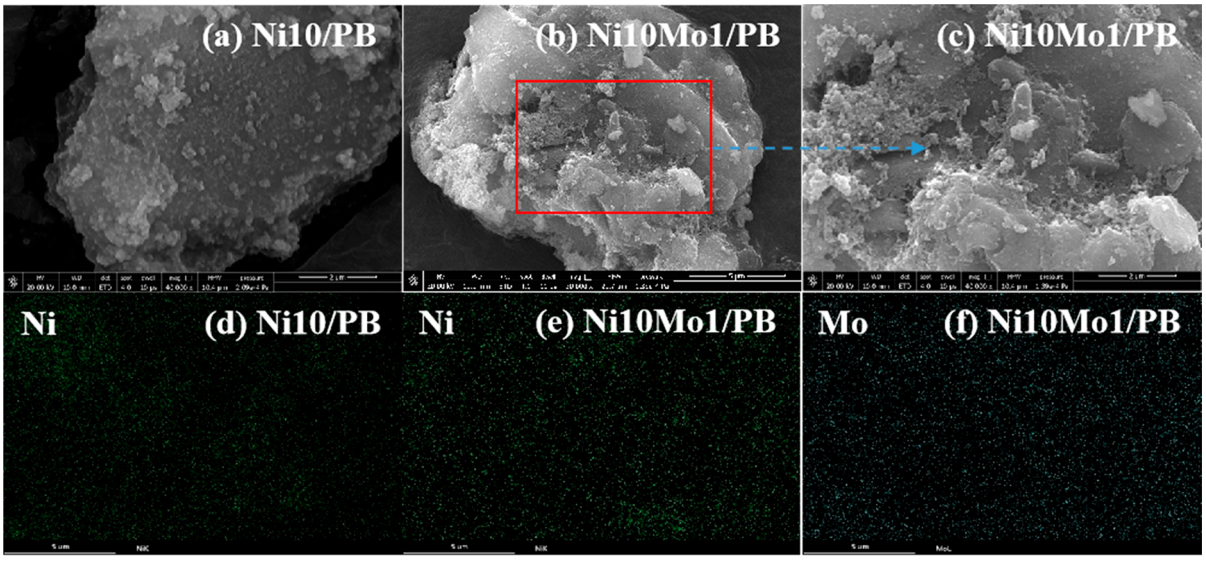


**Figure 4.** SEM images and particle size distributions. (a) Ni10/PB, (b) Ni10Mo1/PB, and (c) Ni10Mo1/PB EDX images. (d) Ni in Ni10/PB, (e) Ni in Ni10Mo1/PB, and (f) Mo in Ni10Mo1/PB



https://doi.org/10.1021/acsomega.2c01742
ACS Omega 2022, 7, 27172−27184

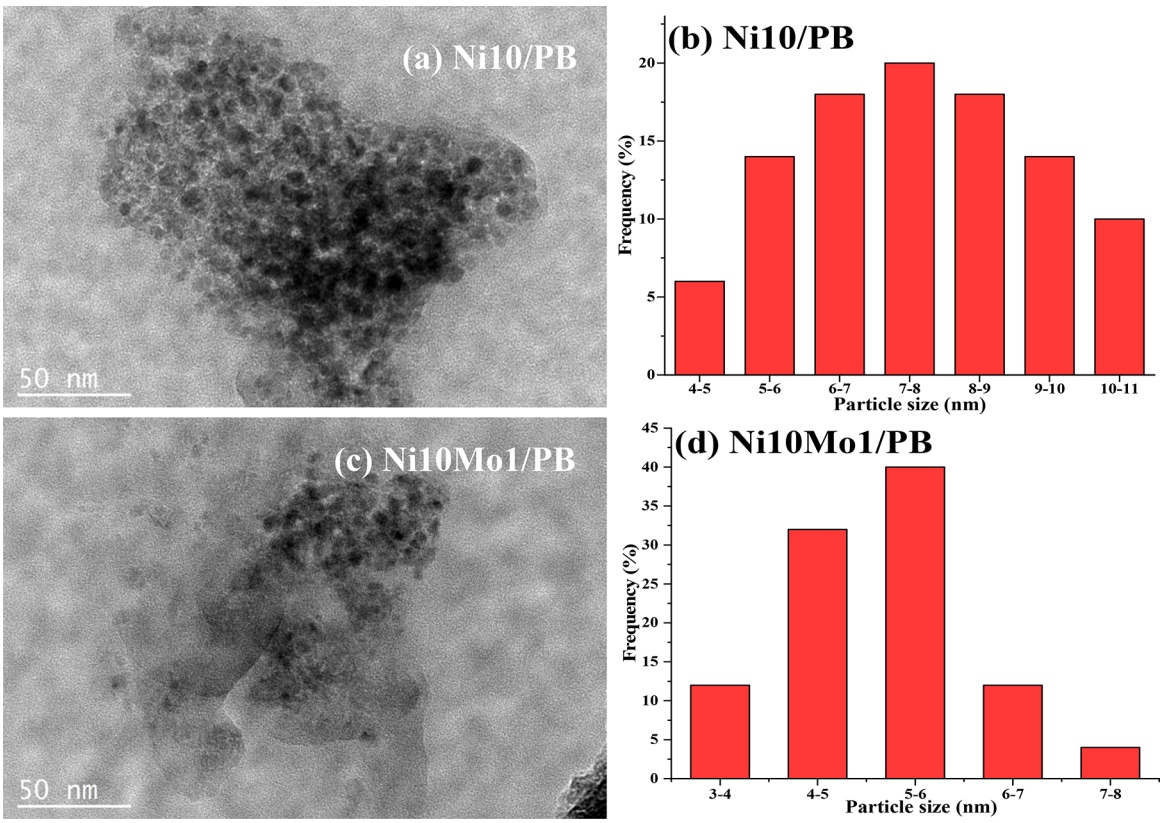


**Figure 5.** TEM images and particle size distributions. (a) Ni10/PB. (b) Histogram frequency for Ni10/PB. (c) Ni10Mo1/PB. (d) Histogram frequency for Ni10Mo1/PB.

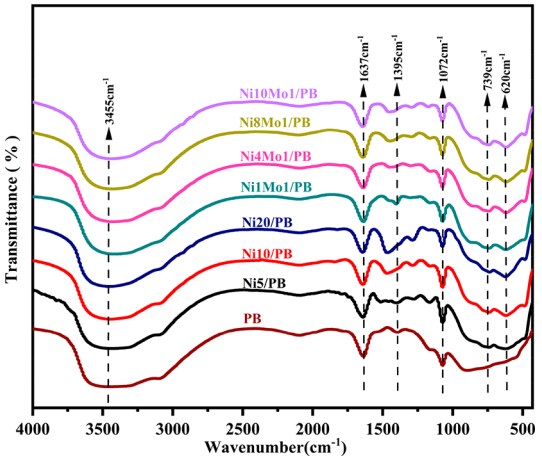


**Figure 6.** FTIR spectra of Ni/PB and NiMo/PB.

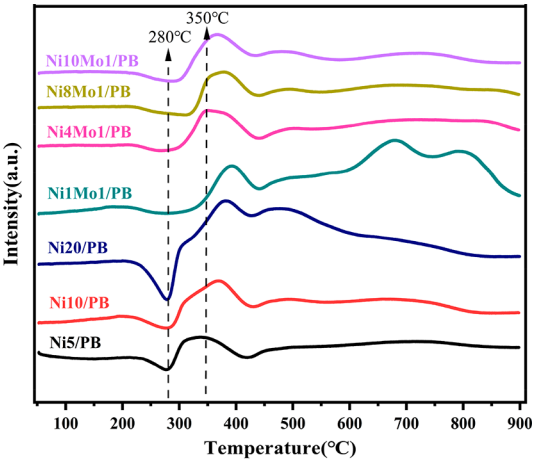


**Figure 7.** $H_2$-TPR profiles of Ni/PB and NiMo/PB.

content increases. For NiMo/PB, the peak gradually shifts to the right as the Ni/Mo ratio decreases. This indicates that the increase in Mo content enhances the interaction of NiO on PB. The reduction of Mo is usually divided into two steps:[49] one reduction peak located at 600−800 °C is the low-temperature reduction peak of Mo, where $Mo^{6+}$ is reduced to $Mo^{4+}$, and the other reduction peak at 800−900 °C is the high-temperature reduction peak of Mo, where $Mo^{4+}$ is reduced to $Mo^{0}$. The special peak of Ni1Mo1/PB at 600−900 °C is due to the increased intensity at 600−900 °C caused by more Mo content.

The acidity of the catalysts has an important effect on the catalytic performance. $NH_3$ can be absorbed in the acidic position of the catalysts. Therefore, $NH_3$-temperature-programmed desorption ($NH_3$-TPD) was performed to test the acidity of Ni/PB and NiMo/PB. There are three types of $NH_3$ desorption peaks located at 130, 230, and 350 °C, which are sequentially assigned to weak, medium, and strong acidic positions.[48] As shown in Figure 8, the Ni10Mo1/PB catalysts have an obvious peak at 423 °C, and it belongs to strong acidic positions. With an increase in Mo content, the peak position at 423 °C shifts to the right, which indicates that the addition of Mo forms more acidic sites on the catalyst surface.

The interactions in Ni/PB and NiMo/PB are further investigated by X-ray photoelectron spectroscopy (XPS) characterization, and Ni 2p, Mo 3d, and Al 2p spectra are shown in Figure 9. Figure 9b shows the XPS spectra of Ni 2p; the



https://doi.org/10.1021/acsomega.2c01742
ACS Omega 2022, 7, 27172−27184

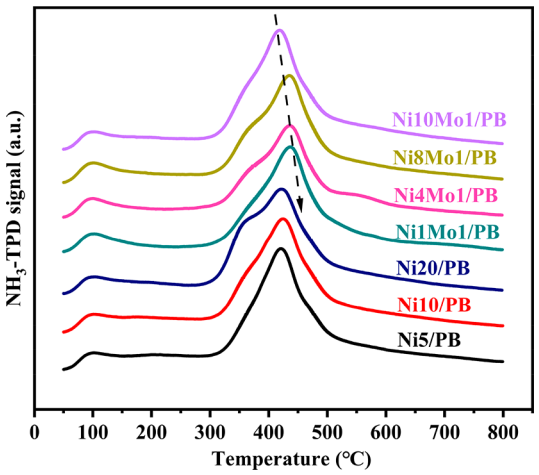


**Figure 8.** $NH_3$-TPD profiles of Ni/PB and NiMo/PB.

peak near 857 eV is associated with Ni $2p_{3/2}$, and the peak near 874 eV is associated with Ni $2p_{1/2}$, which have corresponding satellite peaks at 862 and 880 eV, respectively (sat.). According to previous reports, the binding energy of Ni $2p_{3/2}$ at about 854 eV is associated with a large amount of isolated NiO, while the binding energy at 857 eV is associated with a strong interaction of $Ni^{2+}$ and PB.[29] The 854 eV peak is not found in the spectra, indicating that the isolated NiO species has been completely reduced to the Ni species.[27] $Ni^{2+}$ species found in the range 857−871 eV are Ni species reacting with PB to form Ni−O−Al solid solutions; the peaks associated with $Ni^{2+}$ species increased significantly with increasing Ni content, indicating that the PB interaction with Ni species formed more Ni−O−Al solid solutions, and Ni−O−Al solid solutions formed through the interplay of Ni with the PB play a key role in catalytic performance.[47] Based on the study of $Mo^{4+}$ $3d_{3/2}$ (231.81 eV), $Mo^{6+}$ $3d_{5/2}$, and $Mo^{6+}$ $3d_{3/2}$ (232.82 and 235.13 eV), Mo 3d spectra (Figure 10c) can be divided into three subpeaks.[50] To further confirm the formation of Ni−O−Al solid solution, the XPS spectra of Al 2p are shown in Figure 9d; the peak at about 73 eV belongs to the aluminum metal phase (Al), while the peak at 75 eV belongs to the fully oxidized aluminum substance ($Al_2O_3$).[28,51] In Figure 9d, all catalysts have a main peak at about 74.4 eV. This peak does not belong to the Al metallic phase or $Al_2O_3$ phase but belongs to the Al−O linkage formed through the $Al^{3+}$ species at the octahedral sites of the PB skeleton binding with the O species in PB. The central position of the Al 2p spectra is shifted to high BE values with increasing Ni content. Distinctively, this phenomenon is more predominant in Ni10Mo1/PB, further validating that there are more Ni−O−Al species in Ni10Mo1/PB.[28]

**2.2. Catalytic Performance Test.** Figure 10 shows the FA conversion rate, $H_2$ yield, $H_2$ selectivity, and carbon-containing product selectivity for Ni/PB catalysts (Ni5/PB, Ni10/PB, and Ni20/PB) in the hydrogen production experiments from formic acid. With an increase in Ni content from 5 to 10 wt %, the FA conversion rate increases from 27.8% to 82.1%. When the Ni

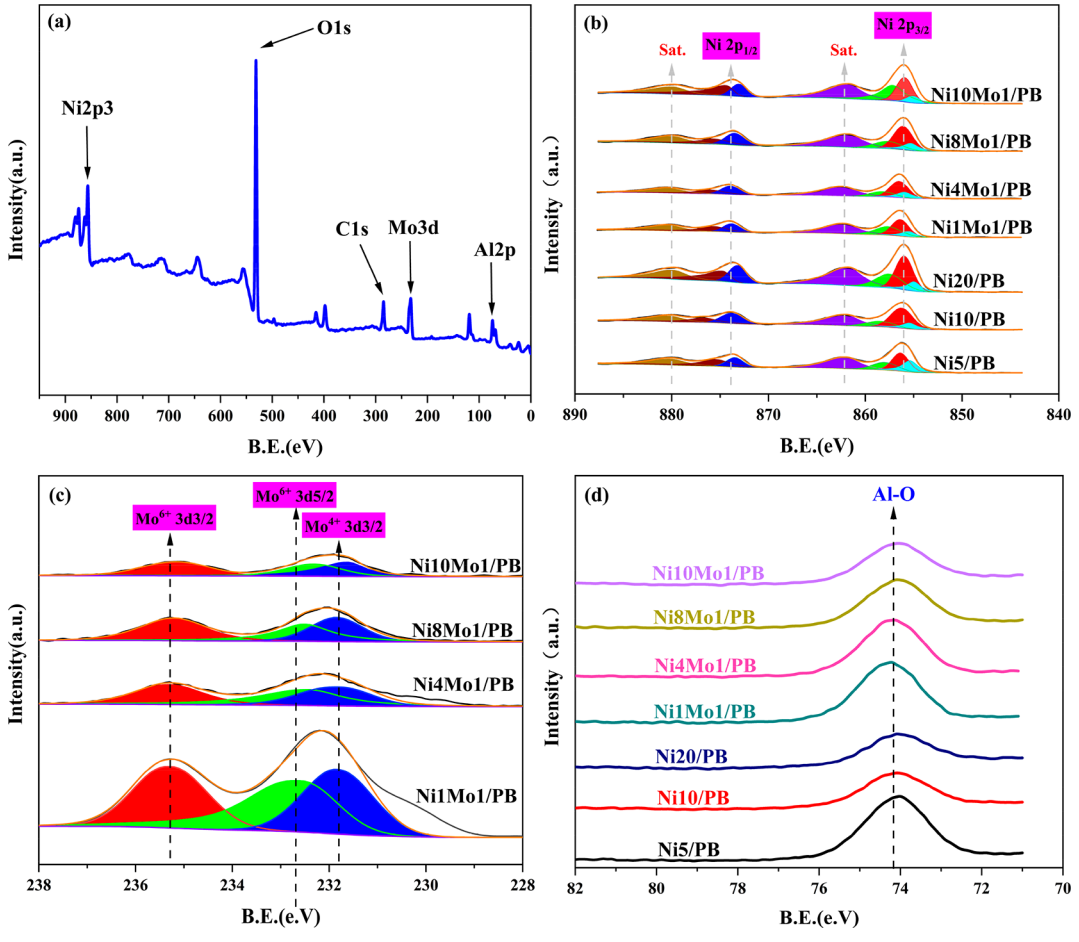


**Figure 9.** XPS spectra of Ni/PB and NiMo/PB. (a) XPS survey spectrum, (b) Ni 2p, (c) Mo 3d, and (d) Al 2p.



https://doi.org/10.1021/acsomega.2c01742
ACS Omega 2022, 7, 27172−27184

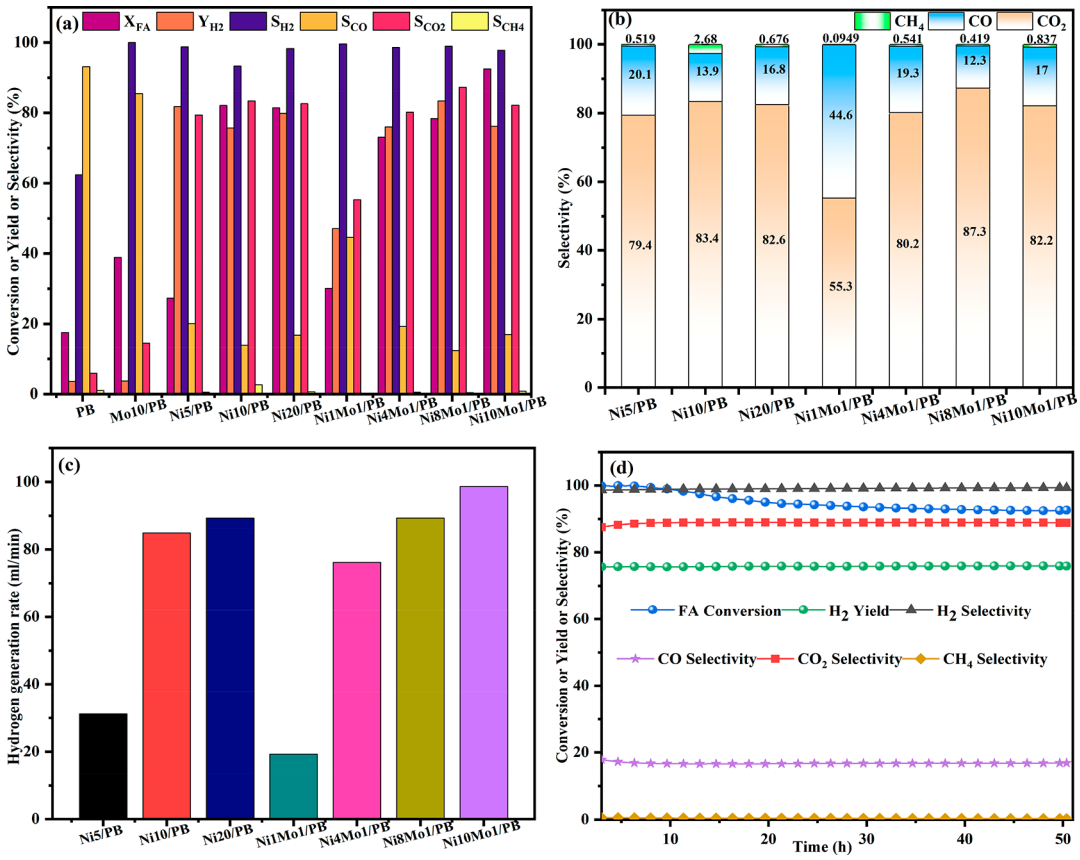


**Figure 10.** (a) FA conversion rate ($X_{FA}$), $H_2$ yield ($Y_{H_2}$), and $CH_4$/CO/$CO_2$ selectivity of Ni/PB and NiMo/PB. (b) Carbon-containing product selectivity. (c) $H_2$ production rate. (d) Ni10Mo1/PB stability test.

**Table 2. Research Progress of Non-Noble Metal Catalysts for Hydrogen Production from Formic Acid**

| | reaction conditions | | | | | |
|---|---|---|---|---|---|---|
| catalyst type | carrier gas flow rate (mL/min) | formic acid concentration (%) | reaction temperature (°C) | formic acid conversion (%) | hydrogen selectivity (%) | ref |
| NiCu/NCNT | 25 | 5.5 | 180−210 | 100 | 94−98 | 19 |
| Ni/CN-1073 | 67 | 2.5 | 300 | 61 | 97 | 55 |
| Soy−Mo (0.1) | 50 | | 110 | 100 | | 24 |
| $MoS_2$/graphene | 51 | 1.8 | 235 | 92 | 42 | 56 |
| Ni/Ca(19.3)−$SiO_2$ | 25 | 6 | 160 | 100 | 92 | 57 |
| Ni−Cu/K | 25 | 6 | 130 | 100 | 95 | 58 |
| 7.5% Co/MWCNT | 20 | 5 | 300 | 100 | 85 | 21 |
| 1Ni/C | 67 | 2.5 | 300 | 40 | 95−97 | 59 |
| Ni10Mo1/PB | 200 | 41 | 300 | 92.8 | 98 | |

content is 20 wt %, the FA conversion rate decreases slightly to 81.4%. The $H_2$ yields of Ni5/PB and Ni20/PB are 81.8% and 80%, respectively. The $H_2$ yield of Ni10/PB decreased to 75.7%. With an increase in the Ni content, the FA conversion rate increases gradually, while the $H_2$ yield decreases with an increase in FA conversion rate. However, compared with Ni10/PB, the FA conversion rate of Ni20/PB decreases slightly, only changing by 0.7%, while the $H_2$ yield increases from 75.7% to 80%. The Ni10/PB catalyst shows the highest FA conversion rate, mainly because it has the smallest active metal particle size and the largest active metal surface area, which can provide more active sites for the reaction process of hydrogen production from formic acid.[52] Therefore, in the following experiments, Ni10/PB is modified to improve the catalyst performance.

Figure 10 shows the catalyst performance with different Ni/Mo ratios (1:1, 4:1, 8:1, and 10:1). An increase in the Ni/Mo ratio can improve the FA conversion rate and $H_2$ yield. The FA conversion rate of Ni10Mo1/PB is 92.8%, and the $H_2$ yield first increases and then decreases with an increase in the Ni/Mo ratio. The $H_2$ yield of Ni8Mo1/PB reaches a maximum of 83.4%. The increase in the FA conversion rate and $H_2$ yield is mainly due to the decrease in Ni particle size, which provides more active sites for hydrogen production from formic acid.[53] The above characterization methods have demonstrated that the addition of Mo significantly reduces the Ni particle size and increases the interaction between Ni and PB. In addition, the effects of various catalysts on the carbon-containing product selectivity are shown in Figure 10b. The $CH_4$ selectivity


https://doi.org/10.1021/acsomega.2c01742
ACS Omega 2022, 7, 27172−27184

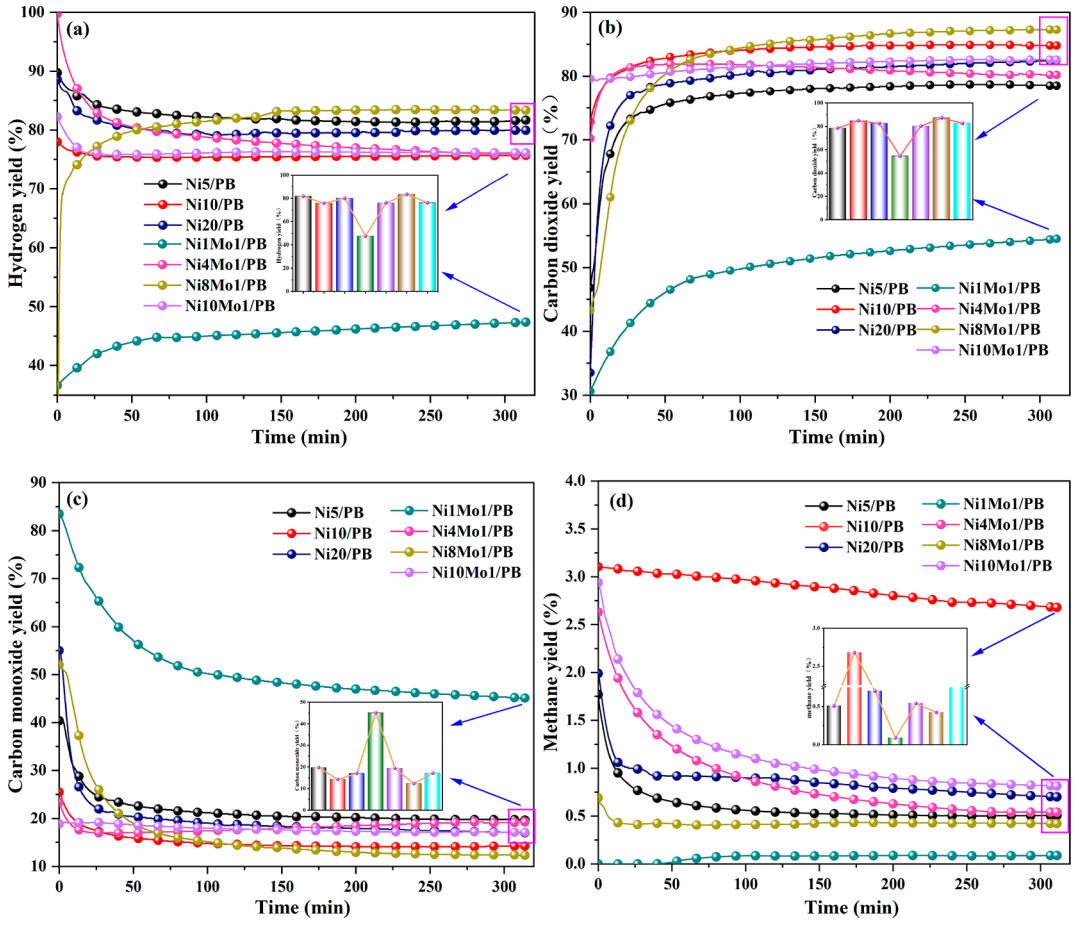


**Figure 11.** Gas yield of Ni/PB and NiMo/PB catalysts: (a) hydrogen, (b) carbon dioxide, (c) carbon monoxide, and (d) methane.

gradually increases with an increase in Ni/Mo ratio, and the $CH_4$ selectivity reaches a minimum of 0.095% for the Ni1Mo1/PB catalyst; the $CH_4$ selectivity of the Ni10Mo1/PB catalyst reaches a maximum of 0.83%. The $CH_4$ in the product is produced by a methanation reaction ($CO + 3H_2 = CH_4 + H_2O$). Therefore, it can be assumed that the increase in Mo content can inhibit the methanation reaction. The change trend of $CO_2$ selectivity is consistent with that of $H_2$ selectivity, while the change trend of CO selectivity is to decrease and then increase. The $H_2$ production rate increases with increases in the Ni/Mo ratio (Figure 10c). The average $H_2$ production rate of the Ni10Mo1/PB catalyst for 6 h reaches 99 mL/min. In addition, the hydrogen production experiment from formic acid is carried out without catalyst, and formic acid shows no decomposition phenomenon. The catalytic phenomenon of PB and Mo10/PB is studied: the PB catalyst shows low activity (Figure 10a), and the FA conversion rate is 17.5% and CO selectivity 93.1%. Mo10/PB has a higher activity than PB, and the FA conversion rate is 38.9% and CO selectivity 85.5%; this phenomenon is also observed by Chiang et al.[54] Therefore, it can be inferred that Ni can promote formic acid decomposition toward the dehydrogenation path.

The currently reported research progress of nonprecious metal catalysts for the hydrogen production reaction from formic acid is summarized in Table 2. Carrales-Alvarado et al. prepared a series of Ni/Cu-based catalysts using different nanostructural carbon materials as carriers, investigated the effect of N doping on the catalyst performance, and found that formic acid reached complete conversion at 180−210 °C and that hydrogen selectivity was 94−98%.[19] Bulusheva et al. reported the effect of Ni/carbon on hydrogen production from formic acid and found that, at 300 °C, the conversion rate of FA was 60%, and the hydrogen selectivity was 96%.[55] Junli Wang et al. synthesized a high-performance Mo-based catalyst using soybean and molybdate. When the soybean and molybdate ratio was 1:0.1, the obtained catalyst had an excellent performance, and formic acid could be completely transformed at 110 °C.[24] Bulushev et al. deposited $MoS_2$ on graphene flakes by decomposition of $MoS_3$ in vacuum conditions at different temperatures (500−800 °C) as a catalyst for hydrogen production from formic acid and found that the conversion rate of formic acid was 92%, and hydrogen selectivity was 42% at 235 °C.[56] Rodríguez-Ramos et al. investigated the catalysts of Ni and Ca supported $SiO_2$ for hydrogen production from formic acid and found that the hydrogen selectivity was 94.5%.[57] Faroldi et al. synthesized Ni, Cu, and Ni−Cu catalysts loaded with high-specific-surface-area graphite by the impregnation method and investigated the effect of alkali metal (Li, Na, and K) doping. The bimetallic Ni−Cu catalyst had the best catalytic performance; the formic acid reached complete conversion, and hydrogen selectivity was 95% at 130 °C.[58] Kazakova et al. prepared catalysts of Co loaded on carbon nanotubes for hydrogen production from formic acid. At 300 °C, they found that the conversion rate of FA was close to 100% for of 7.5% Co/MWCNT, but the hydrogen selectivity was low (85%).[21] Bulushev et al. prepared Ni/C single-atom catalysts; the conversion rate of FA was 40% at 350 °C, and the hydrogen selectivity was 95−97%.[59] The conversion rate of FA was


https://doi.org/10.1021/acsomega.2c01742
ACS Omega 2022, 7, 27172−27184

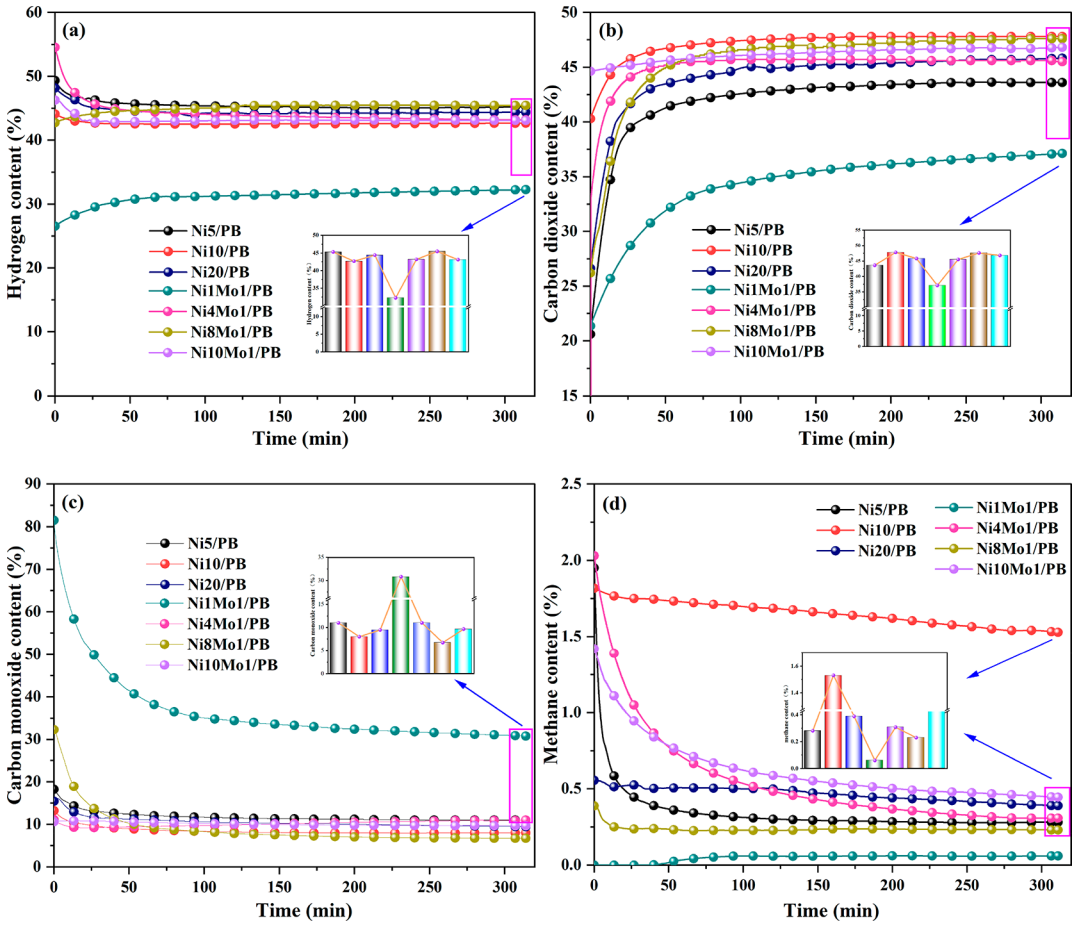


**Figure 12.** Gas content of gas yield of Ni/PB and NiMo/PB: (a) hydrogen, (b) carbon dioxide, (c) carbon monoxide, and (d) methane.

significantly lower than the results in this paper, which may be due to the low active metal content for the single-atom catalyst. Compared with the above catalysts, the Ni10Mo1/PB catalyst in this paper exhibited an excellent catalytic performance. Since the catalyst stability is an important factor in assessing the feasibility of industrial applications for hydrogen production reactions from formic acid, the catalyst stability was tested. Figures 11−13 show the gas yield, gas content, and gas selectivity of Ni/PB and NiMo/PB in the hydrogen production reaction from formic acid. Ni/PB and NiMo/PB always maintain an excellent catalytic performance in the 6 h catalytic reaction. In addition, the stability of Ni10Mo1/PB is tested for 50 h; the FA conversion, $H_2$ yield, and carbon-containing product selectivity almost remain constant, indicating that Ni10Mo1/PB possesses excellent stability during 50 h of reaction.

**2.3. Mechanism Analysis of Formic Acid Decomposition.** The mechanism of formic acid decomposition is shown in Figure 14. The C═O double bond energy in the FA molecule is much larger than the C—H and O—H bonds,[60−62] so there are generally two paths for FA decomposition. One is that the O—H bond of FA breaks to produce HCOO* and H*, and the C—H bond of HCOO* breaks to produce $CO_2$ and H*. Then, H* combines with H* to form $H_2$. The other path is that the C—H bond of FA breaks to produce COOH* and H*, and the C—O bond of COOH* breaks to produce CO and OH*; then, OH* combines with H* to form $H_2O$. COOH* may also break the O—H bond to form $CO_2$ and H*, and then, $H_2$ is produced. However, the O—H bond of COOH* has a larger bond energy relative to the C—H bond,[63] so it is easier for COOH* to produce CO. Therefore, the ideal direction for the hydrogen production reaction from FA is HCOOH → HCOO* + H* → $CO_2$ + H* + H* → $CO_2$ + $H_2$. The $CH_4$ is obtained from the methanation reaction of $H_2$ and CO.

## 3. CONCLUSIONS

In conclusion, Mo-modified pseudoboehmite supported Ni catalysts have been prepared and evaluated for hydrogen production from formic acid. It was found that both the PB textural properties and Mo-promoter had significant roles in the catalytic performance. The PB textural structure was beneficial to obtain small Ni particles, and Mo led to the generation of oxygen vacancies, enhancing Ni anchoring and thus inhibiting Ni sintering. The Ni/PB and NiMo/PB had mesoporous structures, and the pore size distributions were mainly concentrated between 2 and 20 nm. Compared with Ni10/PB (7.62 nm), Ni10Mo1/PB had a smaller Ni particle size (5.08 nm). The Ni−O−Al solid solutions formed through the interaction of Ni with PB, which improved the catalytic performance. Ni10Mo1/PB gave the highest conversion of 92.8% with a $H_2$ selectivity of 98% at 300 °C, and the catalyst activity hardly decreased during the 50 h stability test. Therefore, Ni10Mo1/PB was a promising catalyst for hydrogen production from formic acid.

## 4. EXPERIMENTAL SECTION

**4.1. Catalyst Preparation.** A series of Ni/PB catalysts with different Ni contents (5%, 10%, and 20%) were prepared by the chemical reduction method. 3 g of PB and a certain amount of Ni



https://doi.org/10.1021/acsomega.2c01742
ACS Omega 2022, 7, 27172−27184

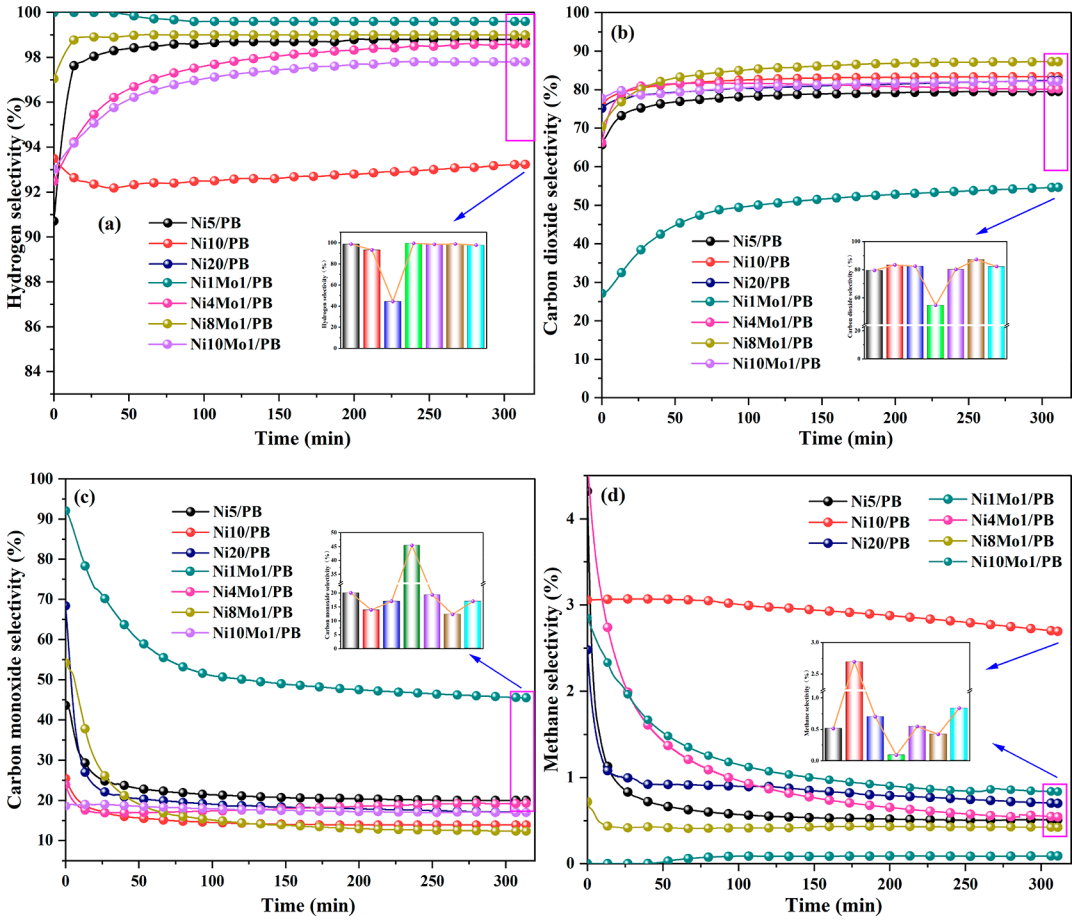


**Figure 13.** Gas selectivity of Ni/PB and NiMo/PB: (a) hydrogen, (b) carbon dioxide, (c) carbon monoxide, and (d) methane.

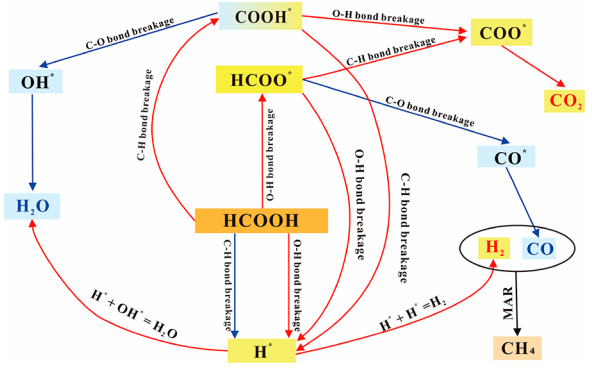


**Figure 14.** Reaction mechanisms of HCOOH decomposition.

$(NO_3)_2{\cdot}6H_2O$ (0.78, 1.65, and 3.72 g) were added into 300 mL of deionized water and stirred for 3 h. A certain amount of $NaBH_4$ (1.01, 2.15, and 4.83 g) was dissolved in 100 mL of deionized water. After it was completely dissolved, $NaBH_4$ aqueous solution was dropped into the above suspension at a rate of 2 mL/min. After that, the solution was stirred for 1 h. Then, the catalysts were centrifuged and washed three times with deionized water. Finally, the catalysts were dried at 60 °C in a vacuum oven for 12 h. The catalysts are named Ni5/PB, Ni10/PB, and Ni20/PB according to the different Ni contents.

A series of Ni−Mo/PB catalysts with different Ni/Mo ratios (1:1, 4:1, 8:1, and 10:1) were prepared by the chemical reduction method, in which the total mass of Ni and Mo accounted for 10% of the total mass of the catalysts. 3 g of PB and certain amounts of Ni $(NO_3)_2{\cdot}6H_2O$ and $(NH_4)_6Mo_7O_{24}{\cdot}4H_2O$ were added into 300 mL of deionized water and stirred for 3 h. A certain concentration of an aqueous solution of $NaBH_4$ (1.70, 1.96, 2.03, and 2.05 g; 100 mL of deionized water) was dropped into the above suspension at a rate of 2 mL/min. The following steps were similar to that of Ni/PB catalysts. The catalysts are named Ni1Mo1/PB, Ni4Mo1/PB, Ni8Mo1/PB, and Ni10Mo1/PB according to the different Ni/Mo ratios.

**4.2. Catalytic Test.** Catalytic activity tests were carried out in a fixed-bed flow reactor with continuous feeding, as shown in Figure 15. First, the catalyst wrapped in quartz cotton was placed in the center of the reaction tube, and the oxidizing gas in the reaction tube was removed by a 200 mL/min $N_2$ flow. Then, the reaction tube was heated to 300 °C, and the feed rate of formic acid (0.23 mL/min) was controlled by a constant flow peristaltic pump using 200 mL/min $N_2$ as the carrier gas. The produced gas is cooled by a flowing water cooler to remove the condensable components. The composition and content of the gas were detected by a portable flue gas analyzer (Gasboard-3100). The FA conversion rate ($X_{FA}$), $H_2$ yield ($Y_{H_2}$), $H_2$ selectivity ($S_{H_2}$), and carbon-containing products selectivity ($S_i$) are determined by the following formula:



https://doi.org/10.1021/acsomega.2c01742
ACS Omega 2022, 7, 27172−27184

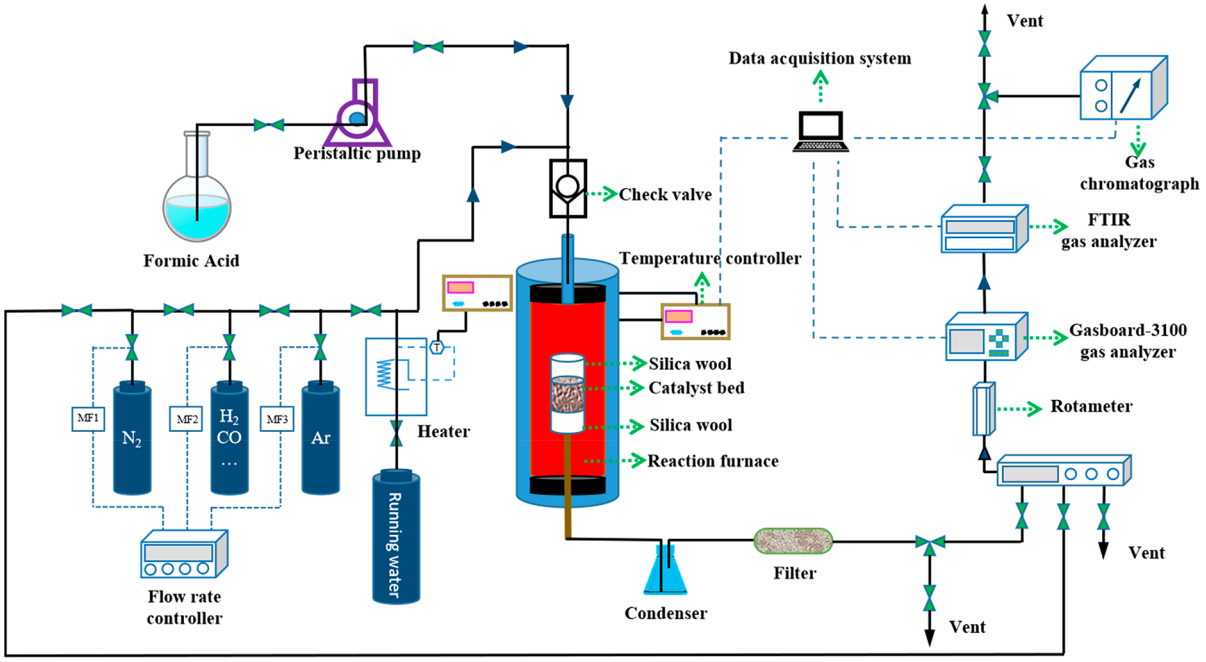


**Figure 15.** Diagram of the experimental setup.

$$X_{FA} = \frac{\text{molar amount of formic acid actually reacted}}{\text{molar amount of formic acid feed}} \times 100\%$$

$$Y_{H_2} = \frac{\text{molar amount of hydrogen produced}}{\text{molar amount of formic acid feed} \times X_{FA}} \times 100\%$$

$$S_{H_2} = \frac{\text{molar amount of hydrogen produced}}{\text{molar amount of hydrogen produced} + 2 \times \text{molar amount of methane produced}} \times 100\%$$

$$S_i = \frac{\text{molar amount of i produced}}{\text{molar amount of formic acid feed}} \times 100\%$$

where i stands for CO, $CO_2$, or $CH_4$.

**4.3. Catalyst Characterization.** The amount of the active metal was analyzed with an XRF spectrometer (ZSX-100e, Rigaku Corporation). The determination conditions were as follows: Rh target; element range B−U; 7−148° scan; tube voltage of 60 kV; and tube current of 150 mA. The XRD patterns were recorded by a Rigaku Corporation SmartLab (3 kW) X-ray diffractometer utilizing Cu K$\alpha$ radiation ($\lambda$ = 0.154 056 nm) over 5−80° at 40 kV and 40 mA. Fourier transform infrared spectroscopy (FTIR) was conducted on a Nicolet 5700 spectrometer in 4000−400 $cm^{-1}$ with a resolution of 2 $cm^{-1}$.

SEM images were obtained on a Quanta 250 FEI microscope operating at 20.0 kV. TEM images were carried out by an FEI Tecnai G2 F20 transmission electron microscope at an operating voltage of 200 kV. The particle size of the active metal was obtained using Nano Measurer 1.2 software (Beijing Zhongke Baice Technology Service Co., LTd, Beijing, China). Additionally, the average particle size was statistically calculated by measuring more than 100 uniform particles from several selected TEM images.

The $N_2$ adsorption−desorption isotherms were recorded by a surface area and porosity analyzer (JW-BK200C). Prior to the measurements, all catalysts were preheated to 250 °C for 4 h under a vacuum. The reduction behavior and metal−carrier interactions of the catalysts were evaluated by $H_2$-TPR experiments on an AutoChemII 2920 instrument. First, about 10 mg of sample was pretreated at 200 °C for 2 h under a 40 mL/min Ar flow to remove the adsorbed moisture and then cooled down to 50 °C. Second, the sample was heated up to 900 °C at 10 °C/min under a 40 mL/min 5% $H_2$/Ar flow. The effluent gas was forced into the thermal conductivity detector (TCD) to detect the hydrogen consumption. $NH_3$-TPD was conducted to evaluate the surface acidity of the catalysts on an AutoChem II 2920 instrument. The catalysts were heated up to 300 °C at 10 °C/min under a 30 mL/min He flow and kept at 300 °C for 1 h to remove the adsorbed volatile substances. Then, a mixture of 5% $NH_3$/He was administered to saturate the surface. The physically adsorbed $NH_3$ was removed by a 30 mL/min He flow for 1 h at 50 °C. Then, the sample was heated to 800 °C at 10 °C/min under a He flow to desorb the chemisorbed $NH_3$.

All XPS measurements were performed by a Thermo Fisher Scientific ESCALAB 250Xi spectrometer using monochrome Al K$\alpha$ (1486.68 eV) radiation as the excitation source under a vacuum of 0 mbar. The spectrometer was operated at 150 W and utilized a 500 $\mu$m beam spot. The obtained binding energies (BEs) were corrected using the 284.8 eV signal of adventitious hydrocarbon C 1s.



https://doi.org/10.1021/acsomega.2c01742
ACS Omega 2022, 7, 27172−27184

## AUTHOR INFORMATION


### Corresponding Authors

**Peng Fu** − *School of Agricultural Engineering and Food Science, Shandong University of Technology, Zibo 255000, China;* orcid.org/0000-0002-2436-0401; Email: fupengsdut@163.com

**Zhiyu Li** − *School of Agricultural Engineering and Food Science, Shandong University of Technology, Zibo 255000, China;* Email: tarimlizhiyu@hotmail.com

### Authors

**Liang Zheng** − *School of Agricultural Engineering and Food Science, Shandong University of Technology, Zibo 255000, China*

**Fazhe Sun** − *Analytical Testing Center, Shandong University of Technology, Zibo 255000, China*

**Mingyang Liu** − *School of Agricultural Engineering and Food Science, Shandong University of Technology, Zibo 255000, China*

**Tianyang Guo** − *School of Agricultural Engineering and Food Science, Shandong University of Technology, Zibo 255000, China*

**Qingwen Fan** − *School of Agricultural Engineering and Food Science, Shandong University of Technology, Zibo 255000, China;* orcid.org/0000-0001-5612-1846

Complete contact information is available at: https://pubs.acs.org/10.1021/acsomega.2c01742


### Notes

The authors declare no competing financial interest.

## ACKNOWLEDGMENTS

This work was supported by National Natural Science Foundation of China (51976112), China Postdoctoral Science Foundation (2021M691969), and Jiangmen Innovation Practice Postdoctoral Research Project (JMBSH2021C03).

## REFERENCES


(1) Rezaei, M.; Chermahini, A. N. A DFT study on production of hydrogen from biomass-derived formic acid catalyzed by Pt-TiO2. *Int. J. Hydrogen Energy.* **2020**, *45*, 20993−21003.

(2) Fu, P.; Bai, X.; Yi, W.; Li, Z.; Li, Y. Fast pyrolysis of wheat straw in a dual concentric rotary cylinder reactor with ceramic balls as recirculated heat carrier. *Energy Convers. Manage.* **2018**, *171*, 855−862.

(3) Fu, P.; Yi, W.; Li, Z.; Li, Y. Comparative study on fast pyrolysis of agricultural straw residues based on heat carrier circulation heating. *Bioresour. Technol.* **2019**, *271*, 136−142.

(4) Fu, P.; Bai, X.; Li, Z.; Yi, W.; Li, Y.; Zhang, Y. Fast pyrolysis of corn stovers with ceramic ball heat carriers in a novel dual concentric rotary cylinder reactor. *Bioresour. Technol.* **2018**, *263*, 467−474.

(5) Zhang, Z.; Luo, Y.; Liu, S.; Yao, Q.; Qing, S.; Lu, Z. H. A PdAg-$CeO_2$ nanocomposite anchored on mesoporous carbon: a highly efficient catalyst for hydrogen production from formic acid at room temperature. *J. Mater. Chem. A* **2019**, *7*, 21438−21446.

(6) Choi, B. S.; Song, J.; Song, M.; Goo, B. S.; Lee, Y. W.; Kim, Y.; Yang, H.; Han, S. W. Core-shell engineering of Pd-Ag bimetallic catalysts for efficient hydrogen production from formic acid decomposition. *ACS Catal.* **2019**, *9*, 819−826.

(7) Tedsree, K.; Li, T.; Jones, S.; Chan, C. W. A.; Yu, K. M. K.; Bagot, P. A.; Marquis, E. A.; Smith, G. D. W.; Tsang, S. C. E. Hydrogen production from formic acid decomposition at room temperature using a Ag-Pd core-shell nanocatalyst. *Nat. Nanotechnol.* **2011**, *6*, 302−307.

(8) Zhong, S.; Tsumori, N.; Kitta, M.; Xu, Q. Immobilizing palladium nanoparticles on boron-oxygen-functionalized carbon nanospheres towards efficient hydrogen generation from formic acid. *Nano Res.* **2019**, *12*, 2966−2970.

(9) Yao, M.; Liang, W.; Chen, H.; Zhang, X. Efficient hydrogen production from formic acid using nitrogen-doped activated carbon supported Pd. *Catal. Lett.* **2020**, *150*, 2377−2384.

(10) Barlocco, I.; Capelli, S.; Zanella, E.; Chen, X.; Delgado, J. J.; Roldan, A.; Dimitratos, D.; Villa, A. Synthesis of palladium-rhodium bimetallic nanoparticles for formic acid dehydrogenation. *J. Energy Chem.* **2021**, *52*, 301−309.

(11) Solymosi, F.; Koós, A.; Liliom, N.; Ugrai, I. Production of CO-free $H_2$ from formic acid. A comparative study of the catalytic behavior of Pt metals on a carbon support. *J. Catal.* **2011**, *279*, 213−219.

(12) Luo, Y.; Yang, Q.; Nie, W.; Yao, Q.; Zhang, Z.; Lu, Z. H. Anchoring IrPdAu Nanoparticles on $NH_2$-SBA-15 for Fast Hydrogen Production from Formic Acid at Room Temperature. *ACS Appl. Mater. Interfaces.* **2020**, *12*, 8082−8090.

(13) Santucci, M.; Ermini, M. L.; Bresciani, G.; Griesi, A.; Gemmi, M.; Pampaloni, G.; Marchetti, F.; Voliani, V. Total-and semi-bare noble metal nanoparticles@ silica core@ shell catalysts for hydrogen generation by formic acid decomposition. *Emergent Mater.* **2021**, *4*, 483−491.

(14) Wang, Z. L.; Yan, J. M.; Wang, H. L.; Ping, Y.; Jiang, Q. Pd/C synthesized with citric acid: an efficient catalyst for hydrogen generation from formic acid/sodium formate. *Sci. Rep.* **2012**, *2*, 1−6.

(15) Hattori, M.; Einaga, H.; Daio, T.; Tsuji, M. Efficient hydrogen production from formic acid using TiO2-supported AgPd@Pd nanocatalysts. *J. Mater. Chem. A* **2015**, *3*, 4453−4461.

(16) Caiti, M.; Padovan, D.; Hammond, C. Continuous production of hydrogen from formic acid decomposition over heterogeneous nanoparticle catalysts: From batch to continuous flow. *ACS Catal.* **2019**, *9*, 9188−9198.

(17) Du, Y.; Shen, Y. B.; Zhan, Y. L.; Ning, F. D.; Yan, L. M.; Zhou, X. C. Highly active iridium catalyst for hydrogen production from formic acid. *Chin. Chem. Lett.* **2017**, *28*, 1746−1750.

(18) Iglesia, E.; Boudart, M. Decomposition of formic acid on copper, nickel, and copper-nickel alloys. III., Catalytic decomposition on nickel and copper-nickel alloys. *J. Catal.* **1983**, *81*, 224−238.

(19) Carrales-Alvarado, D. H.; López-Olmos, C.; Dongil, A. B.; Kubacka, A.; Guerrero-Ruiz, A.; Rodríguez-Ramos, I. Effect of N-doping and carbon nanostructures on NiCu particles for hydrogen production from formic acid. *Appl. Catal., B* **2021**, *298*, 120604.

(20) Bulushev, D. A.; Chuvilin, A. L.; Sobolev, V. I.; Stolyarova, S. G.; Shubin, Y. V.; Asanov, I. P.; Ishchenko, A. V.; Magnani, G.; Riccò, M.; Okotrub, A. V.; Bulusheva, L. G. Copper on Carbon Materials: Stabilization by Nitrogen Doping. *J. Mater. Chem. A* **2017**, *5*, 10574−10583.

(21) Kazakova, M. A.; Selyutin, A. G.; Ishchenko, A. V.; Lisitsyn, A. S.; Koltunov, K. Y.; Sobolev, V. I. Co/multi-walled carbon nanotubes as highly efficient catalytic nanoreactor for hydrogen production from formic acid. *Int. J. Hydrogen Energy.* **2020**, *45*, 19420−19430.

(22) Koroteev, V. O.; Bulushev, D. A.; Chuvilin, A. L.; Okotrub, A. V.; Bulusheva, L. G. Nanometer-sized $MoS_2$ clusters on graphene flakes for catalytic formic acid decomposition. *ACS Catal.* **2014**, *4*, 3950−3956.

(23) Li, L.; Tang, D.; Song, Y.; Jiang, B.; Zhang, Q. Hydrogen production from ethanol steam reforming on Ni-Ce/MMT catalysts. *Energy.* **2018**, *149*, 937−943.

(24) Wang, J.; Li, X.; Zheng, J.; Cao, J.; Hao, X.; Wang, Z.; Abudula, A.; Guan, G. Non-precious molybdenum-based catalyst derived from biomass: CO-free hydrogen production from formic acid at low temperature. *Energy Convers. Manage.* **2018**, *164*, 122−131.

(25) Chen, M.; Hu, J.; Wang, Y.; Wang, C.; Tang, Z.; Li, C.; Liang, D.; Cheng, W.; Yang, Z.; Zhang, H. Hydrogen production from acetic acid steam reforming over Ti-modified Ni/Attapulgite catalysts. *Int. J. Hydrogen Energy.* **2021**, *46*, 3651−3668.

(26) Pu, J.; Nishikado, K.; Wang, N.; Nguyen, T. T.; Maki, T.; Qian, E. W. Core-Shell Nickel Catalysts for the Steam Reforming of Acetic Acid. *Appl. Catal., B* **2018**, *224*, 69−79.

(27) Wang, Y.; Wang, C.; Chen, M.; Tang, Z.; Yang, Z.; Hu, J.; Zhang, H. Hydrogen production from steam reforming ethanol over Ni/




https://doi.org/10.1021/acsomega.2c01742
*ACS Omega* 2022, 7, 27172−27184

attapulgite catalysts - Part I: Effect of nickel content. *Fuel Process. Technol.* **2019**, *192*, 227−238.
(28) Tan, M.; Wang, X.; Wang, X.; Zou, X.; Ding, W.; Lu, X. Influence of calcination temperature on textural and structural properties, reducibility, and catalytic behavior of mesoporous γ-alumina-supported Ni-Mg oxides by one-pot template-free route. *J. Catal.* **2015**, *329*, 151−166.
(29) Tan, M.; Wang, X.; Hu, Y.; Shang, X.; Zhang, L.; Zou, X.; Ding, W.; Lu, X. Influence of nickel content on structural and surface properties, reducibility and catalytic behavior of mesoporous γ-alumina-supported Ni-Mg oxides for pre-reforming of liquefied petroleum gas. *Catal. Sci. Technol.* **2016**, *6*, 3049−3063.
(30) Pu, J.; Nishikado, K.; Wang, N.; Nguyen, T. T.; Maki, T.; Qian, E. W. Core-Shell Nickel Catalysts for the Steam Reforming of Acetic Acid. *Appl. Catal., B* **2018**, *224*, 69−79.
(31) Wang, Y.; Chen, M.; Yang, Z.; Liang, T.; Liu, S.; Zhou, Z.; Li, X. Bimetallic Ni-M (M= Co, Cu and Zn) supported on attapulgite as catalysts for hydrogen production from glycerol steam reforming. *Appl. Catal., A* **2018**, *550*, 214−227.
(32) Han, Y.; Wen, B.; Zhu, M.; Dai, B. Lanthanum incorporated in MCM-41 and its application as a support for a stable Ni-based methanation catalyst. *J. Rare Earths.* **2018**, *36*, 367−373.
(33) Shen, K.; Wang, X.; Zou, X.; Wang, X.; Lu, X.; Ding, W. Pre-reforming of liquefied petroleum gas over nickel catalysts supported on magnesium aluminum mixed oxides. *Int. J. Hydrogen Energy.* **2011**, *36*, 4908−4916.
(34) Chen, M.; Li, X.; Wang, Y.; Wang, C.; Liang, T.; Zhang, H.; Yang, Z.; Zhou, Z.; Wang, J. Hydrogen generation by steam reforming of tar model compounds using lanthanum modified Ni/sepiolite catalysts. *Energy Convers. Manage.* **2019**, *184*, 315−326.
(35) Zhao, L.; Jia, J.; Yang, Z.; Yu, J.; Wang, A.; Sang, Y.; Zhou, W.; Liu, H. One-step synthesis of CdS nanoparticles/$MoS_2$ nanosheets heterostructure on porous molybdenum sheet for enhanced photocatalytic $H_2$ evolution. *Appl. Catal., B* **2017**, *210*, 290−296.
(36) Men, Y.; Yang, M. SMSI-like behavior and Ni promotion effect on NiZnAl catalysts in steam reforming of methanol. *Catal. Commun.* **2012**, *22*, 68−73.
(37) Lin, C.-L.; Kuo, J.-H.; Wey, M.-Y.; Chang, S.-H.; Wang, K.-S. Inhibition and promotion: the effect of earth alkali metals and operating temperature on particle agglomeration/defluidization during incineration in fluidized bed. *Power Technol.* **2009**, *189*, 57−63.
(38) Chen, M.; Wang, Y.; Yang, Z.; Liang, T.; Liu, S.; Zhou, Z.; Li, X. Effect of Mg-modified mesoporous Ni/Attapulgite catalysts on catalytic performance and resistance to carbon deposition for ethanol steam reforming. *Fuel.* **2018**, *220*, 32−46.
(39) Lin, C. L.; Kuo, J. H.; Wey, M. Y.; Chang, S. H.; Wang, K. S. Inhibition and promotion: the effect of earth alkali metals and operating temperature on particle agglomeration/defluidization during incineration in fluidized bed. *Powder Technol.* **2009**, *189*, 57−63.
(40) Zhang, G.; Xiong, T.; Yan, M.; He, L.; Liao, X.; He, C.; Yin, C.; Zhang, H.; Mai, L. α-$MoO_3$-x by plasma etching with improved capacity and stabilized structure for lithium storage. *Nano Energy.* **2018**, *49*, 555−563.
(41) Rahmani, F.; Haghighi, M.; Vafaeian, Y.; Estifaee, P. Hydrogen production via $CO_2$ reforming of methane over $ZrO_2$-Doped Ni/ZSM-5 nanostructured catalyst prepared by ultrasound assisted sequential impregnation method. *J. Power Sources.* **2014**, *272*, 816−827.
(42) Fu, P.; Yi, W.; Li, Z.; Bai, X.; Wang, L. Evolution of char structural features during fast pyrolysis of corn straw with solid heat carriers in a novel V-shaped down tube reactor. *Energy Convers. Manage.* **2018**, *171*, 855−862.
(43) Jamalzadeh, Z.; Haghighi, M.; Asgari, N. Synthesis, physicochemical characterizations and catalytic performance of Pd/carbon-zeolite and Pd/carbon-$CeO_2$ nanocatalysts used for total oxidation of xylene at low temperatures. *Front. Environ. Sci. Eng.* **2013**, *7*, 365−381.
(44) Zheng, Q.; Zhang, D.; Fu, P.; Wang, A.; Sun, Y.; Li, Z.; Fan, Q. Insight into the fast pyrolysis of lignin: Unraveling the role of volatile evolving and char structural evolution. *Chem. Eng. J.* **2022**, *437*, 135316.
(45) Khoshbin, R.; Haghighi, M.; Asgari, N. Direct synthesis of dimethyl ether on the admixed nanocatalysts of CuO-ZnO-$Al_2O_3$ and $HNO_3$-modified clinoptilolite at high pressures: Surface properties and catalytic performance. *Mater. Res. Bull.* **2013**, *48*, 767−777.
(46) Zhang, G.; Liu, J.; Xu, Y.; Sun, Y. Ordered mesoporous Ni/Silica-carbon as an efficient and stable catalyst for $CO_2$ reforming of methane. *Int. J. Hydrogen Energy.* **2019**, *44*, 4809−4820.
(47) Li, B.; Lin, X.; Luo, Y.; Yuan, X.; Wang, X. Design of active and stable bimodal nickel catalysts for methane reforming with $CO_2$. *Fuel Process. Technol.* **2018**, *176*, 153−166.
(48) Abdollahifar, M.; Haghighi, M.; Babaluo, A. A.; Talkhoncheh, S. K. Sono-synthesis and characterization of bimetallic Ni-Co/$Al_2O_3$-MgO nanocatalyst: Effects of metal content on catalytic properties and activity for hydrogen production via $CO_2$ reforming of $CH_4$. *Ultrason. Sonochem.* **2016**, *31*, 173−183.
(49) Men, Y.; Yang, M. SMSI-like behavior and Ni promotion effect on NiZnAl catalysts in steam reforming of methanol. *Catal. Commun.* **2012**, *22*, 68−73.
(50) Wang, Y.; Tang, Z.; Chen, M.; Zhang, J.; Shi, J.; Wang, C.; Yang, Z.; Wang, J. Effect of Mo content in Mo/Sepiolite catalyst on catalytic depolymerization of Kraft lignin under supercritical ethanol. *Energy Convers. Manage.* **2020**, *222*, 113227.
(51) Tang, P.; Chai, Y.; Feng, J.; Feng, Y.; Li, Y.; Li, D. Highly dispersed Pd catalyst for anthraquinone hydrogenation supported on alumina derived from a pseudoboehmite precursor. *Appl. Catal., A* **2014**, *469*, 312−319.
(52) Pompeo, F.; Santori, G.; Nichio, N. N. Hydrogen and/or syngas from steam reforming of glycerol. Study of platinum catalysts. *Int. J. Hydrogen Energy.* **2010**, *35*, 8912−8920.
(53) Zhao, X.; Lu, G. Modulating and controlling active species dispersion over Ni-Co bimetallic catalysts for enhancement of hydrogen production of ethanol steam reforming. *Int. J. Hydrogen Energy.* **2016**, *41*, 3349−3362.
(54) Prabu, S.; Chiang, K. Y. Yolk-shell silica dioxide spheres@ metal-organic framework immobilized Ni/Mo nanoparticles as an effective catalyst for formic acid dehydrogenation at low temperature. *J. Colloid Interface Sci.* **2021**, *604*, 584−595.
(55) Nishchakova, A. D.; Bulushev, D. A.; Stonkus, O. A.; Asanov, I. P.; Ishchenko, A. V.; Okotrub, A. V.; Bulusheva, L. G. Effects of the Carbon Support Doping with Nitrogen for the Hydrogen Production from Formic Acid over Ni Catalysts. *Energies.* **2019**, *12*, 4111.
(56) Koroteev, V. O.; Bulushev, D. A.; Chuvilin, A. L.; Okotrub, A. V.; Bulusheva, L. G. Nanometer-Sized $MoS_2$ Clusters on Graphene Flakes for Catalytic Formic Acid Decomposition. *ACS Catal.* **2014**, *4*, 3950−3956.
(57) Faroldi, B.; Paviotti, M. A.; Camino-Manjarrés, M.; González-Carrazán, S.; López-Olmos, C.; Rodríguez-Ramos, I. Hydrogen Production by Formic Acid Decomposition over Ca Promoted Ni/$SiO_2$ Catalysts: Effect of the Calcium Content. *Nanomaterials.* **2019**, *9*, 1516.
(58) Faroldi, B. M.; Conesa, J. M.; Guerrero-Ruiz, A.; Rodríguez-Ramos, I. Efficient nickel and copper-based catalysts supported on modified graphite materials for the hydrogen production from formic acid decomposition. *Appl. Catal., A* **2022**, *629*, 118419.
(59) Bulushev, D. A.; Nishchakova, A. D.; Trubina, S. V.; Stonkus, O. A.; Asanov, I. P.; Okotrub, A. V.; Bulusheva, L. G. Ni-$N_4$ sites in a single-atom Ni catalyst on N-doped carbon for hydrogen production from formic acid. *J. Catal.* **2021**, *402*, 264−274.
(60) Zhang, R.; Yang, M.; Peng, M.; Ling, L.; Wang, B. Understanding the role of Pd: Cu ratio, surface and electronic structures in Pd-Cu alloy material applied in direct formic acid fuel cells. *Appl. Surf. Sci.* **2019**, *465*, 730−739.
(61) Wang, P.; Steinmann, S. N.; Fu, G.; Michel, C.; Sautet, P. Key role of anionic doping for $H_2$ production from formic acid on Pd(111). *ACS Catal.* **2017**, *7*, 1955−1959.
(62) He, F.; Li, K.; Xie, G.; Wang, Y.; Jiao, M.; Tang, H.; Wu, Z. Understanding the enhanced catalytic activity of Cu-1@Pd-3(111) in formic acid dissociation, a theoretical perspective. *J. Power Sources.* **2016**, *316*, 8−16.


https://doi.org/10.1021/acsomega.2c01742
*ACS Omega* 2022, 7, 27172−27184

(63) Yoo, J. S.; Abild-Pedersen, F.; Nørskov, J. K.; Studt, F. Theoretical Analysis of Transition-Metal Catalysts for Formic Acid Decomposition. *ACS Catal.* **2014**, *4*, 1226−1233.



https://doi.org/10.1021/acsomega.2c01742
*ACS Omega* 2022, 7, 27172−27184